THE JOURNAL OF PHYSICAL CHEMISTRY C

Article

pubs.acs.org/JPCC

Plasmon Mediated Multiphoton Photoemission Microscopy of Au Nanoholes and Nanohole Dimers

Thomas A. Baker, Andrej Grubisic, and David J. Nesbitt*

JILA, University of Colorado and National Institute of Standards and Technology, and Department of Chemistry and Biochemistry, University of Colorado, Boulder, Colorado 80309 United States

ABSTRACT: Multiphoton photoemission from "nanoholes" and "nanohole dimers" fabricated by nanosphere shadow lithography in a thin Au film are investigated by ultrafast scanning photoionization microscopy (SPIM), which provides detailed information on laser polarization and local electric field enhancement effects for novel 2D plasmonic architectures. The net photoemission signals (at 800 nm) from *isotropic* nanohole monomers both (i) below ($d \ll \lambda$) and (ii) comparable to ($d \approx \lambda$) the diffraction limit are insensitive to laser polarization, though SPIM images of the larger species clearly reveal strongly enhanced electron emission from nanohole tangent edges *perpendicular* to incident laser polarization. Fundamentally contrasting behavior is observed for intrinsically *anisotropic* plasmonic architectures such as nanohole *dimers*. Specifically, small nanohole dimers reveal enhanced electron emission for λ = 800 nm light polarized *perpendicular* to the dimer axis, whereas larger nanohole dimers produce optimum electron yields for polarization *parallel* to the dimer axis at the same excitation wavelength. We find excellent agreement between the SPIM images for the four classes of nanostructures and detailed finite element simulations for photoemission, where the latter include (i) the spatial dependence of the electric field enhancement around the nanoobject and (ii) diffraction limited spatial resolution of the laser source. In general, these studies highlight multiphoton photoemission of nanoholes and nanohole aggregates as sensitive benchmark systems for imaging local plasmonic field enhancements, which enables detailed characterization of nanobjects far below the diffraction limit.

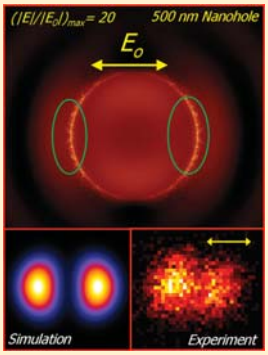

I. INTRODUCTION

Metallic nanoparticle systems display qualitatively different optical properties from those observed in the bulk. In particular, optical extinction spectra of nanoparticles can reveal highly structured resonance behavior, in spite of its complete absence in samples of macroscopic dimensions. In addition to their unique optical properties, these nanoscale metal materials also possess many interesting electronic properties. Synthetic and sample preparation techniques have progressed to a degree that permits study of the size and shape dependence for ensemble properties such as absorption and fluorescence emission spectra of noble metal nanoparticles.[1−4] The choice of the noble metals, predominately silver and gold, is motivated by the presence of strong surface plasmon resonances (SPR) in the near-ultraviolet and visible range, which reflect excitation of a collective electron oscillation. The convenience of visible laser excitation, coupled with the strong size, shape and proximity dependence of the spectral properties, makes these metal nanoparticles a logical target for a broad spectrum of research and commercial applications.[5−10]

Such plasmonic behavior not only influences far field measurements such as absorption and scattering but also impacts the highly local electric fields in the sub-diffraction limited vicinity of the nanoparticle. For example, this local enhancement of electric fields has been used to enable Raman characterization at the single molecule limit by surface enhanced Raman scattering (SERS).[9,11−15] The influence of plasmonic excitation on multiphoton processes has also been studied. Specifically, second harmonic generation has been observed to be enhanced by metal nanostructures due to the intense local electric fields generated upon excitation.[16−19] Indeed, multiphoton processes are intrinsically more sensitive to such nanoscale enhancements due to the highly nonlinear dependence on incident electric field. However, the clean isolation of plasmonic effects due to nanoparticle shape from other contributions (e.g., neighboring nanoparticle proximity, surface roughness, laser frequency, etc.) has remained an ongoing challenge.

It has been long established that plasmonic resonances can significantly increase the rate of *single-photon* photoemission from metal surfaces and particles.[20−22] Recently, *multiple-photon* photoemission (MPPE) studies have begun to examine the role of plasmons in enhancing photoelectron yield from nanostructured materials.[23−30] Indeed, MPPE from metal nanoparticles removes several complications present in other studies (e.g., second harmonic generation), due to the absence of (i) rigorous surface selection rules and (ii) the need for high order electric field susceptibility materials. Specifically, MPPE has been shown to depend sensitively on local electric field enhancements in the nanoparticle near field, which in turn can be rigorously modeled by plasmonic excitation theory.[31−33] This relatively simple combination of MPPE and optical microscopy, therefore, provides a novel access to probing single nanostructures with exquisite single electron counting

Received: December 5, 2013
Revised: February 19, 2014
Published: February 20, 2014

   dx.doi.org/10.1021/jp411943f | *J. Phys. Chem. C* 2014, 118, 6959−6971

sensitivity. A variety of nanostructures have been studied by our group via scanning photoionization microscopy (SPIM), e.g., nanorods,[31,32] nanoshells, and nanocubes,[31,33] which has provided insights into the link between the local electric field and the photoemission yield. Most importantly, it is this powerful connection between (i) near electric field distributions and (ii) flux of emitted photoelectrons that enables probing of sub-diffraction limited *near-field* effects due to nanostructures with an intrinsically *far-field* detection experiment.

By the superposition principle, one can readily extend these ideas of electric field enhancements due to the *presence* of isolated plasmonic nanostructures, to those of plasmonics explicitly arising from the *absence* of nanostructured materials. As the central focus of the present work, we have explored scanning electron photoemission microscopy dynamics of metal "anti-nanoparticles," i.e., strongly plasmonic 2D objects made by shadow lithographic formation of nanoscale *holes* in a thin Au metal film. Based on simple superposition arguments, the resulting vector fields arising from the Au nanohole should be similar in magnitude but opposite in sign for a nanodisk of the same diameter. Indeed, the general linear and nonlinear optical properties of a nanoparticle and the associated "anti-nanoparticle" (i.e., "nanohole") are intimately related,[34−36] though, as this work illustrates, there are also clearly differences in photoemission behavior. Onuta et al. first took advantage of these superposition arguments and nonlinear spectroscopy to investigate large monomer and dimer holes (300−1000 nm diameter) in relatively thick Au films (100−300 nm).[37] In particular, the absence of centrosymmetry at the Au thin film/nanohole interface could be exploited for second harmonic generation (SHG), which yielded spatially localized SHG signals with strong polarization dependences for both monomer and dimer species.

The present work significantly extends both the concept and sensitivity of these previous studies into the ultrafast microscopy domain, specifically probing the plasmonic properties of nanohole monomers and dimers by multiphoton photoemission microscopy. Specifically, we fabricate a thin Au film (height, $h \approx 25$ nm) substrate containing holes with diameters both below ($d \approx 60$ nm) and near ($d \approx 500$ nm) the diffraction limit ($\lambda \approx 700$ nm) by shadow mask lithography using spin cast polystyrene spheres.[38−40] The sizes are chosen to explore how nanohole size and corresponding plasmonic properties influence the photoemission signals, as well as to take advantage of the spatially resolved photoemission microscopy capabilities of the apparatus. Complementary vector information on local electric field enhancements is then also attained by studies as a function of laser polarization. In addition, both small ($d \approx 60$ nm) and large ($d \approx 500$ nm) nanohole dimers are investigated to explore the role of the diffraction limit on spatial, frequency, and polarization sensitivity of the photoemission event.

The paper is organized as follows. Section II presents details of the experimental and theoretical methods, while section III describes photoemission results obtained from isolated nanohole monomers and compares them to computational modeling of the plasmonic electric field enhancement. Section IV presents the corresponding results for spatial and polarization dependent photoemission from nanohole dimers, again correlated with computational predictions of the electric field enhancements. In addition, the observed polarization and spatial dependences are interpreted in the context of a simple model, which assumes appropriate scaling of the 4-photon photoemission signals with (i) local emission area and (ii) eighth power of the local electric field enhancement. Section V further discusses the similarities and differences in photoemission behavior of the related geometries, while section VI summarizes the conclusions and suggests directions for future work.

II. EXPERIMENT

Isolated nanoholes are prepared by a simple shadow mask lithography[10,38,40−43] procedure pictorially depicted in Figure 1.

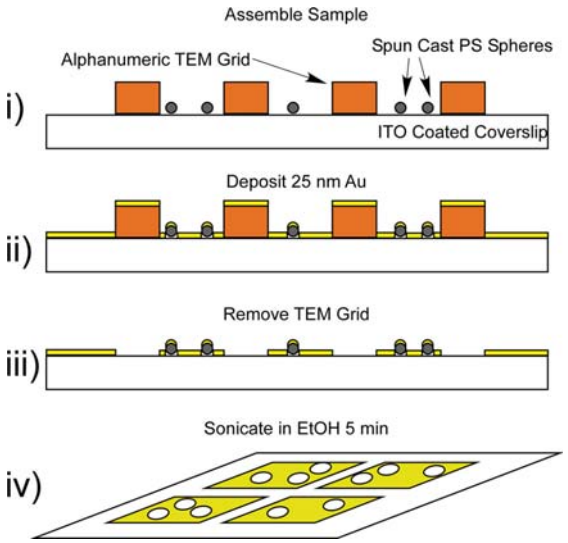

Figure 1. Sample preparation via shadow mask lithography. (i) Polystyrene spheres (PS) are spin cast on an ITO coated coverslip. (ii) Indexed TEM grid is placed on top, and 25 nm of gold is deposited onto the sample. (iii) TEM grid is then removed to expose the registration pattern. (iv) Substrate is sonicated in ethanol for 5 min to remove the PS and leave nanohole monomers (and occasional dimers) in an indexed gold film.

Low concentrations (10^8 #/mL) of carboxylate functionalized polystyrene spheres (Invitrogen) of two different diameters (d = 60 and 500 nm) are first spin cast on an ITO coated glass coverslip (Thin Film Devices, Inc.). An uncoated copper TEM finder grid (EMS, LF400CU) is then secured on top of the coverslip and held in place with magnets. The sample is subsequently placed in a vacuum deposition chamber, where a 25 nm layer of gold is deposited via e-beam assisted vaporization at approximately 1 Å/s. The TEM grid is then carefully removed, with the resulting sample sonicated in ethanol for 5 min to detach the Au-capped PS spheres. The resultant substrate therefore contains isolated Au "nanohole" (and occasional "nanohole dimer") shadows in the Au film, spatially registered with an easily addressable grid. The sample is checked for sufficiently low coverage (typically 0.7 object/μm^2) by dark field scattering before being loaded into the scanning photoionization microscopy (SPIM) chamber.

The SPIM technique is described here in brief, with more detailed information available in the literature.[44,45] The fundamental frequency output from an ultrafast Ti:sapphire laser system ($\lambda \approx 800$ nm, 40 fs pulse width, 90 MHz repetition rate) is focused from below the sample at normal incidence by an all-reflective microscope objective (NA = 0.65) inside a vacuum chamber maintained at $\sim 5 \times 10^{-7}$ Torr. The focus (D

dx.doi.org/10.1021/jp411943f | J. Phys. Chem. C 2014, 118, 6959−6971

$\approx \lambda/(2\mathrm{NA}) \approx 700$ nm) provides a diffraction limited spatial region in which the laser intensity (typically 10^9 W/cm^2 peak) is sufficient to eject electrons via multiphoton photoemission (MPPE). These electrons are then detected by a Channeltron electron multiplier situated ∼1 cm directly above the sample platform, with the spatial region of interest raster-scanned in vacuo by an open loop piezoelectric stage. The reported work function[46] of gold varies considerably in the literature (Φ_{Au} = 4.6−5.1 eV) due to surface preparation. However, for a typical estimate for clean, evaporated Au ($\Phi_{Au} \approx 5$ eV), emission of single photoelectrons energetically requires absorption of four λ = 800 nm photons, which is confirmed by observation of a fourth order dependence of SPIM signal on laser intensity. Tapping mode AFM images of the samples are acquired using a 2−5 nm radius of curvature tip, which provides an invaluable one-to-one correspondence between nanostructure morphology and the observed SPIM signals.

The near-field distribution of electric fields of Au nanoholes and nanodimers is calculated via finite element methods in COMSOL (v4.2), with the predicted local electric field enhancements used to interpret the experimental results. The calculations are based on a three layer slab model composed of (i) a thin Au film containing the desired nanohole architecture, surrounded below and above by (ii) a glass coverslip substrate and (iii) vacuum, respectively. The nanostructured Au film is defined to be oriented in the *xy*-plane and has a thickness of h = 25 nm to match the actual AFM measurements of the sample. The system is discretized using the built-in free meshing algorithm, which defines elements as small tetrahedral regions and produces a mesh based on various user supplied constraints on the sample dimensions. The minimum element edge length is 2 nm in the 60 nm nanohole systems and 5 nm for the 500 nm systems, corresponding to a nanostructure radius of curvature to element ratio between 30:1 and 100:1. For all systems, the maximum element edge lengths were chosen to be 12 nm with a growth rate of 1.2, i.e., adjacent elements could grow at most by 20%. Convergence in these COMSOL predictions has been tested by calculations as a function of mesh sizes (e.g., 2 nm vs 3 nm) for the 60 nm nanoholes. As expected, such comparisons yield uniformly higher electric field enhancement factors for the more finely defined (and thus sharper) edges, but which, outside of overall normalization factor, are indistinguishable as a function of 3D spatial coordinate indicating grid size convergence. The bulk dielectric properties for gold are taken from previously reported tables.[47] Laser excitation at $\lambda \approx 800$ nm is modeled as a linearly polarized plane wave starting in the glass surface and propagating toward vacuum in the *z*-direction. Due to the nanohole monomer/dimer architectural point group, only a single quadrant ($x > 0$, $y > 0$) needs to be calculated, with the other three quadrants given by symmetry considerations. Although even higher cylindrical point group symmetry is clearly available for the nanohole monomer structures, we choose the lower point group to facilitate self-consistent comparison between monomer and dimer nanohole behavior. The boundary conditions for the four sides are each set to properly match the linearly polarized plane wave excitation by being set as either a perfect electric conductor (PEC) or perfect magnetic conductor (PMC).

The simulation proceeds in two stages, similar to a previous study of 3D nanocavities in a solid.[48] In the first step, the electric field is solved for a system comprising only a thin continuous Au film, with the grid mesh points defined as if the nanoholes were present. The resulting solution is found to match the analytic solution for a plane wave impinging on a thin film. The advantage of performing the simulation this way is to guarantee that the incident field is self-consistent at every mesh point, with no numerical artifacts that might arise from an analytic solution being applied to an arbitrary discrete mesh. The resulting electric field is then used as the background field in a scattering calculation, where the desired nanohole geometry is defined, thereby determining the spatial dependence of the electric field enhancement due to the nanohole architecture. The exterior boundary condition for this second simulation step is represented by perfectly absorbing layers that absorb all outgoing waves without reflections. The resulting field enhancements are extracted as 2D slices through relevant planes, typically the topmost surface of the film, and analyzed/processed in Matlab.

III. MONOMERS

A. Experiment. A sample AFM of a Au thin film section containing d = 60 nm nanoholes is shown in Figure 2A, with a scan at higher spatial resolution of an individual nanohole displayed as inset in the upper left corner. The corresponding SPIM image (recorded with circularly polarized light) is shown in Figure 2B, which confirms that the photoemission signal arises primarily from the nanoholes, with a 100-fold lower background signal emitted from the gold film itself. As mentioned above, signals from the nanoholes are found to scale quite closely as I^4 (inset Figure 2B), consistent with the four $\lambda \approx 800$ nm photons needed to overcome the work function for Au ($\Phi_{Au} \approx 5$ eV). The spatial fwhm of the photoemission signal, obtained from a two-dimensional Gaussian fit to the data, is 445(8) nm. The one-photon diffraction limit of $D = 1.22\lambda/(2\ \mathrm{NA}) \approx 750$ nm (NA = 0.65, λ = 800 nm) is 67% larger than observed experimentally, due to the multiphoton nature of the excitation event. Specifically, a Gaussian spot size for an N-photon process scaling with I^N should be approximately $D_n = D/\sqrt{N} \approx 375$ nm, which is much closer to and even slightly smaller (−19%) than the observed experimental value.

As a result of the shadow mask lithography method and uniformity of the polystyrene spheres, the nanohole monomers exhibit a high degree of cylindrical symmetry. By way of confirmation, the photoemission signal strengths for the nanoholes have been explored as a function of incident laser polarization. A subset of these data for d = 60 nm nanoholes is shown in Figure 3 for both circular (B) and four different linear polarizations (C−F), which indicates no preferred dependence on polarization for photoemission current. More quantitatively, we can integrate these signals for the full set of data to obtain the total photoemission rate. The polar plot (in Figure 3G) represents the full polarization data set as a function of linear polarization, which within uncertainty confirms that the emission is independent of the incident laser polarization angle, as expected for a cylindrically symmetric object.

Corresponding studies of the much larger (i.e., nondiffraction limited) d = 500 nm nanoholes provide additionally interesting behavior as a function of laser polarization. First of all, the AFM images are now of sufficiently high resolution to reveal, as anticipated, a nearly perfect circular shape with edges that appear quite smooth down to <5 nm scale. A SPIM image recorded with circularly polarized light is presented immediately below (Figure 4B) and reveals a single broad, cylindrically symmetric feature with a spatial fwhm of 900(30) nm. This is in

dx.doi.org/10.1021/jp411943f | J. Phys. Chem. C 2014, 118, 6959−6971

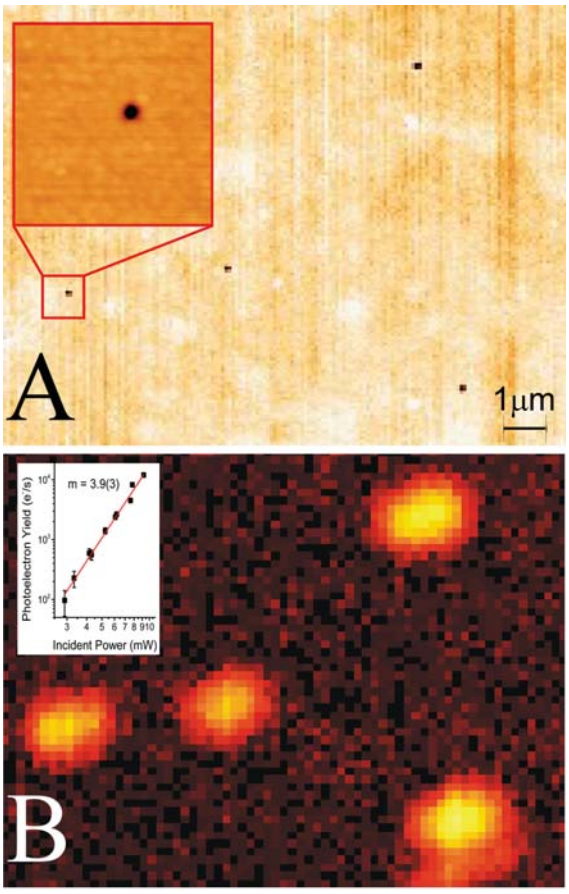

Figure 2. Sample AFM and SPIM images of *small* nanohole monomers with diameter *below* the diffraction limit ($d \approx 60$ nm $\ll \delta$). (A) AFM image: dark and light represent bare ITO substrate and 25 nm thick Au. Inset: 1 μm × 1 μm zoom of an individual nanohole. (B) Correlated SPIM image of the same set of nanoholes recorded with circularly polarized λ = 800 nm light at $I = 1.4 \times 10^{10}$ W/cm^2. Under these conditions typical peak signals and background of 10^6 e$^-$/s and 10^2 e$^-$/s, respectively, are observed. Inset: log–log plot of the photoemission yield versus incident power showing a slope of 3.9(3). This matches the predicted 4 photons necessary to overcome the work function of gold.

reasonably good agreement with expectations, as the SPIM signal arises from the convolution of a cylindrically symmetric top hat function of width 500 nm with a diffraction limited spot size of fwhm ~400 nm. However, a qualitatively different spatial image is observed when this same nanohole feature is investigated with linearly polarized light. Specifically, sample images (shown in Figure 4B–D) reveal that the photoemission signals split into two lobes localized on opposing sides of the 500 nm nanohole, with each lobe exhibiting near diffraction limited fwhms, comparable to 60 nm nanoholes. Interestingly, the two lobes in the SPIM images are always oriented *parallel to* and therefore always *rotate with* the incident linear laser polarization, which will be explored further below with theoretical simulations. Nevertheless, the *integrated* photoemission signal (Figure 4G) is still described by a perfectly isotropic distribution, which is again similar to our previous observation for the 60 nm nanohole samples (see Figure 3). It is worth noting that there is a small increase in the signal at both 90° and 270°, which indicates a deviation from a purely isotropic distribution. Interestingly, this appears to correspond to a slight bump noticeable on the leftmost edge of the AFM as well. The deviation from isotropic is most likely due to this type of fabrication defect and motivates future studies of these structures.

B. Theory. In order to interpret these results, we have implemented a detailed numerical modeling of the experimental signals based on finite element simulations, which permit us to explicitly incorporate plasmonic, laser polarization, and finite spatial resolution effects of the experiment. First of all, the expectation from simple linear superposition arguments is that the spatial distribution of the plasmon (and thus electric field enhancement) around a nanohole should be closely related to that of a nanodisk.[36] Indeed, experiments have shown that the resonances of comparable sized nanodisk and nanohole structures do have similar resonance wavelengths.[34] However, it is worth stressing that this is only rigorously true in the thin film limit for a dipolar plasmon mode. For example, Käll and co-workers have done several optical characterizations of different disk/hole systems and compared their results to a simple electrostatic theory for an oblate spheroid.[34,35,49] In actuality, they find that the true inverse of a *nanodisk* would be a *nanocavity* embedded in a 3D solid, for which the plasmon resonance is strongly *blue-shifted* to higher frequencies. Furthermore, their work has determined that nanoholes and nanodisks have similar resonances simply because the nanohole is unable to support significant polarization in the *z*-direction due to its 2D geometry. This absence of polarizability leads to a correspondingly strong *red-shift* in the plasmon peak, which

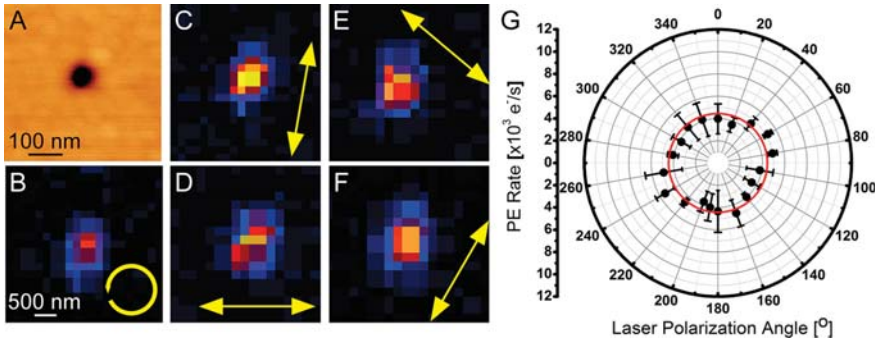

Figure 3. Representative laser polarization dependent photoemission data for a *small* nanohole monomer ($d \approx 60$ nm). (A) 1 μm × 1 μm AFM image of a 60 nm diameter nanohole. SPIM images for circular (B) and a series of linear (C–F) polarization directions indicated by arrows. (G) Polar plot of photoelectron yield as a function of incident polarization angle, revealing a nearly isotropic dependence on laser excitation.

dx.doi.org/10.1021/jp411943f | J. Phys. Chem. C 2014, 118, 6959–6971

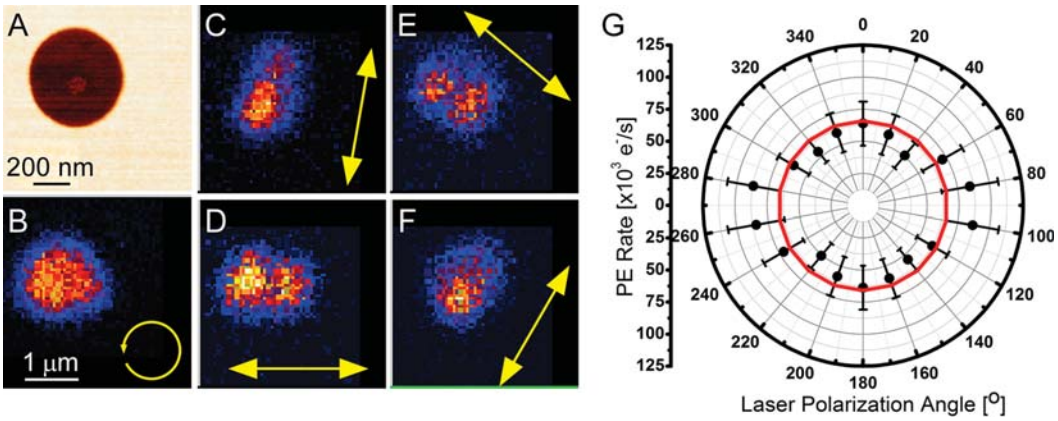

Figure 4. Sample laser polarization dependent photoemission data for a *large* nanohole monomer, with dimensions *comparable* to the diffraction limit ($d \approx 500$ nm $\approx \lambda$). (A) 1 μm × 1 μm AFM image of a 500 nm diameter hole. (B) SPIM image recorded with circularly polarized incident excitation. (C–F) SPIM images recorded with linear polarization. Note that the integrated photoelectron yield as a function of incident polarization (G) is insensitive to the laser polarization axis, despite the clear anisotropy evident in the spatial images.

tends to make thin nanodisks and 2D nanoholes resonate with a more similar plasmon frequency.

Interestingly, the Käll studies also point out that nanoholes should have much *broader* resonances than nanodisks of the same size, which can be attributed to surface plasmon polaritons (SPPs) that provide an additional relaxation pathway present only in nanoholes. SPPs have a decay length that can exceed 10 μm in some 3D systems; however, in thin 2D films, the decay length is found to be much less than 1 μm due to scattering off the nearby glass surface.[49] The presence of a SPP has been found to be particularly relevant for experiments at high nanohole spatial density, where the average distance between objects is less than 500 nm and therefore the holes are optically coupled.[50] In the present samples, however, the average experimental distances between nanoholes are considerably in excess of 1 μm; thus SPP coupling between nanoholes can be neglected, though the spectral resonance of an isolated nanohole should still be slightly broadened.[34]

To facilitate a more detailed comparison with experiment, we model electric fields in the vicinity of a nanohole with finite element electrodynamics simulations, and use these results to accurately predict multiphoton photoemission properties of studied plasmonic nanoarchitectures. In particular, we are interested in the spatial dependence of the local electric field *enhancement*, $\eta_{ENH} = |E/E_0|$, i.e., the ratio of field in the presence of the nanohole to the reference field for a continuous film.[51−53] These enhancement factors are calculated in COMSOL at λ = 800 nm for small (d = 60 nm) and large (d = 500 nm) nanoholes. The results are shown in Figures 5A and 5C, respectively, for an *xy*-slice through the top surface of the film (i.e., h = 25 nm) under various incident laser polarization conditions (depicted schematically in the center row), with intensity scale bars shown on the right-hand side. Interestingly, the plasmonic enhancements are quite similar in each of the two cases, i.e., η_{ENH} is approximately 5-fold larger at opposite edges of the circle where the local tangent is *perpendicular* to the incident polarization compared to the edges for which the local tangent is *parallel* to the incident polarization (Table 1). This immediately explains the lack of any laser polarization sensitivity to the integrated photoemission signals for both nanohole sizes, since circular symmetry always provides nanohole tangent edges pointing in the right direction for such enhancements to promote photoemission. Second, it provides a simple explanation for why the alignment in the spatial images for the larger nanoholes rotates with the laser polarization. Finally, it clearly identifies the essential reason for the absence (d = 60 nm) or presence (d = 500 nm) of spatial variation in the corresponding SPIM images. Specifically, the opposing regions of peak enhancement ($\eta_{ENH} \approx 25$) for the small nanoholes are too close to be resolved, whereas for the larger nanohole species, the sources of photoemission signals are sufficiently far apart to begin contributing independently.

To interpret the observed spatial dependence of the nanohole MPPE images more quantitatively, we propose a model based on the multiphoton nature of the emission that also includes the spatial dependence of the plasmon excitation. In the simplest picture, the observed photoemission yield (PE) will be proportional to the *local* field enhancement raised to the ($2n$)th power (i.e., PE $\propto \eta_{ENH}^{2n}$), where n is the order of the photoemission process, multiplied by the differential area over which these enhanced fields are maintained.[32,33] Therefore, 2D SPIM images can be simulated by a series of calculations at each point in the image. First, the enhancement factor (η_{ENH}) image is multiplied by a Gaussian centered at a given *xy*-coordinate, which represents the incident laser electric field, and yields the map of the local electric field under diffraction-limited illumination. Each pixel in this image map is then raised to the eighth power, due to the 4-photon nature of the photoemission process. Finally the image is integrated to obtain the expected photoemission yield for the laser centered on that *xy*-coordinate. This procedure is repeated on a 2D grid across the feature to generate a map that corresponds to the expected MPPE image. This process is equivalent to convolution of the electric field enhancement factor raised to the eighth power with the Gaussian instrument response function for a diffraction limited 4-photon process (FHWM = 375 nm), which is computationally faster and thus used for the generation of all simulated MPPE spatial images.

The results of these calculations are summarized in Figure 5 for the two different sized nanoholes. In Figure 5A, we present spatial heat maps of $\eta_{ENH}(x,y)$ for small (d = 60 nm) nanoholes at a series of incident laser polarizations, which clearly reveals the synchronous rotation of the field enhanced region with polarization angle. By way of contrast, however, Figure 5B illustrates the spatial convolution of $\eta_{ENH}^8(x,y)$ over the

dx.doi.org/10.1021/jp411943f | J. Phys. Chem. C 2014, 118, 6959−6971

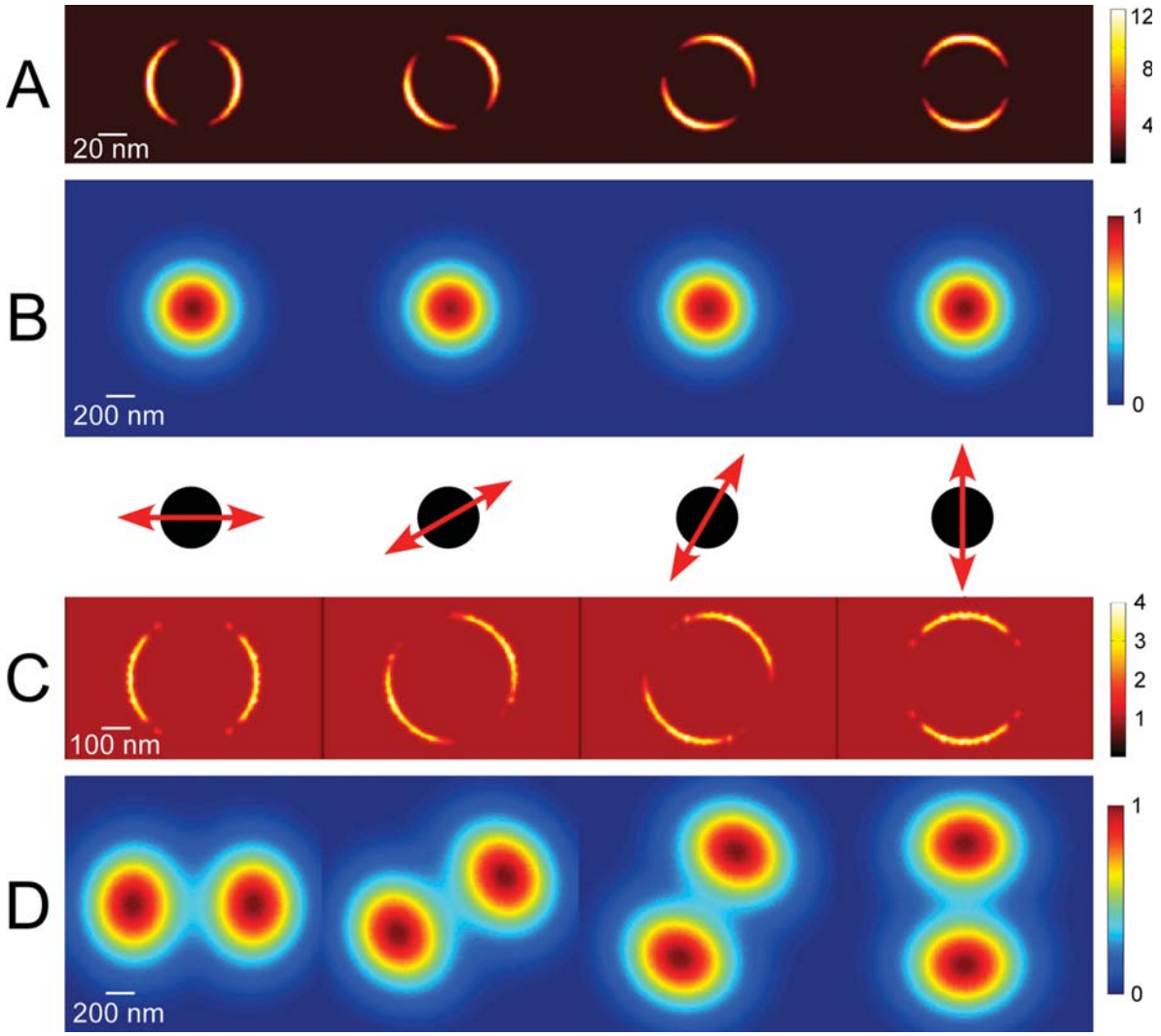

Figure 5. COMSOL predictions for polarization dependence of a *small* ($d \approx 60$ nm $\ll \lambda$) nanohole monomer (upper panels A, B) and a *large* ($d \approx 500$ nm $\approx \lambda$) nanohole monomer (lower panels C, D) for the selected polarizations shown schematically in the middle panel. (A) For small nanohole monomers, the field enhancement factor (η_{ENH}, color scale to right) aligns perfectly parallel with the incident laser, with peak values of $\eta_{ENH} \approx 26$. (B) When modeled by $\eta_{ENH}{}^8$ averaged over the incident 2D electric field distribution, the SPIM predictions (normalized to the maximum value over the full panel) correctly reveal zero anisotropy with respect to laser polarization. For large nanohole monomers, both field enhancement factors (C, peak $\eta_{ENH} \approx 7$) and normalized SPIM signals (D) reveal spatial variations in the images with the same integrated total intensity for each polarization, as expected for cylindrically symmetric nanostructures. See Figure 8 and Tables 1 and 2 for further details and comparisons.

Table 1. Peak COMSOL Field Enhancement Factors for Small ($d \approx 60$ nm $\ll \lambda$) and Large ($d \approx 500$ nm $\approx \lambda$) Nanohole Monomers at Specific Locations for Laser Polarization Perpendicular to the Nanohole Tangent Edge at Point A

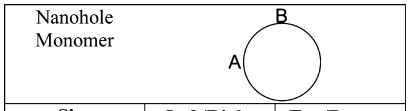

Size	Left/Right Edge (A)	Top/Bottom Edge (B)
Small	**26**	5
Large	**7**	2

instrument response function. Note that the spatial extent of the "hot spot" ridge regions ($\eta_{ENH} \approx 20$) for a $d = 60$ nm nanohole is considerably smaller than the diffraction limit, and thus the image appears as a single diffraction-limited, nearly isotropic spot. For the larger nanoholes, on the other hand, the distance between the opposing hot spot ridge regions in $\eta_{ENH}(x,y)$ is ≈500 nm (see Figure 5C), which makes the predicted photoemission images appear as two readily resolved peaks when excited with a linearly polarized focused laser beam at $\lambda = 800$ nm. Once again, the directional alignment of the two "hot spots" in the enhancement field directly tracks the incident polarization, but they are now at sufficiently large distances to remain resolved after convolution of $\eta_{ENH}{}^8(x,y)$ over the instrument response. As a result, the SPIM images of large Au nanoholes are predicted to exhibit bilobal photoemission spatial patterns that rotate synchronously with laser polarization, in perfect agreement with experimental observations. Furthermore, the separation between peaks is quite uniformly 530(5) nm, which is of course consistent with the 500 nm nanohole size monitored by AFM. In summary, these results clearly

dx.doi.org/10.1021/jp411943f | J. Phys. Chem. C 2014, 118, 6959−6971

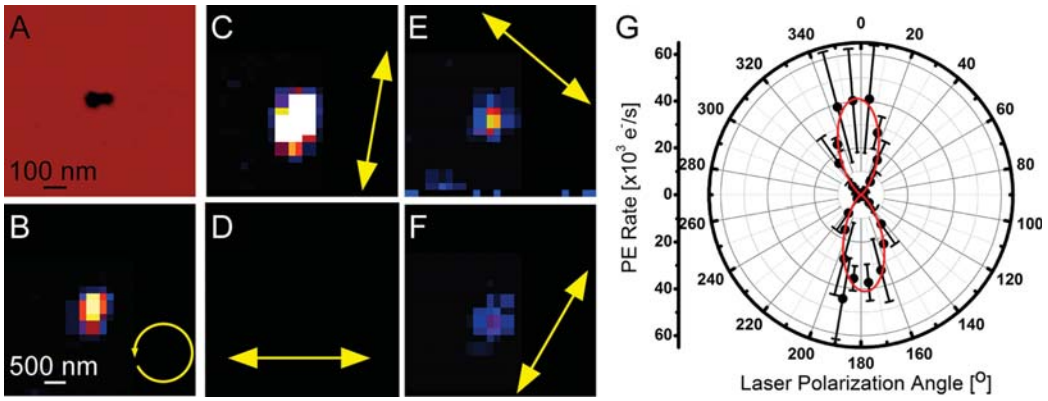

Figure 6. Correlated AFM and SPIM images for a *small* ($d \approx 60$ nm $\ll \lambda$) nanohole dimer. (A) 600 nm × 600 nm AFM image. SPIM images with circular (B) and various linear (C−F) polarizations of incident excitation, each spatially *isotropic* with respect to the nanohole dimer axis. (G) Integrated photoelectron yield as a function of incident laser polarization θ, demonstrating a strong $\cos^8(\theta)$ sensitivity, with strongest photoemission resulting for the electric field vector aligned *perpendicular* to the nanohole dimer axis.

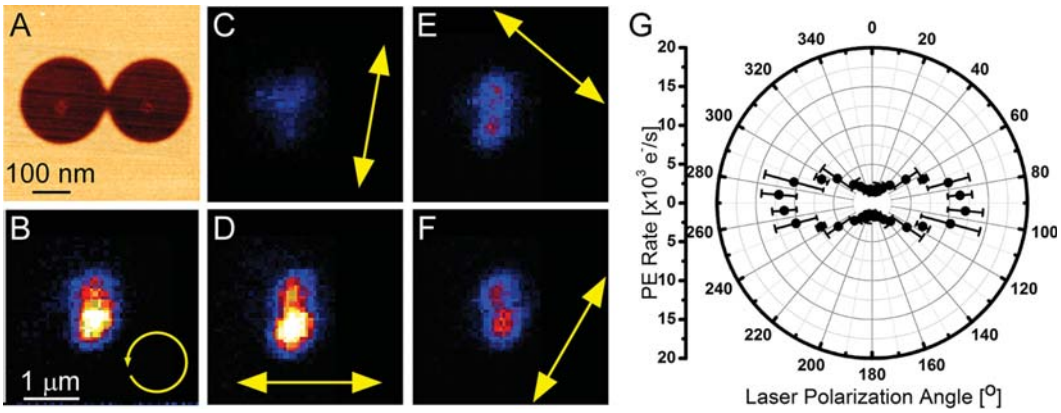

Figure 7. Sample data for a *large* ($d \approx 500$ nm $\approx \lambda$) nanohole dimer. (A) 1.2 μm × 1.2 μm AFM of a 500 nm hole dimer. SPIM image with circular (B) and various linear (C−F) polarization orientations, each spatially *perpendicular* to the nanohole dimer axis. (G) Integrated photoelectron yield as a function of incident laser polarization which reveals a strong $\cos^8(\theta)$ sensitivity *parallel* to the nanohole dimer axis.

indicate that photoemission for both small and large nanohole monomers occurs from the tangent edge regions aligned *perpendicular* to the incident laser polarization, where the electric field enhancement factor is largest.

IV. NANOHOLE DIMERS

A. Experiment. As a rare but welcome accident, two polystyrene spheres occasionally adhere in the spin coating process and fortuitously result in a "nanohole dimer" after deposition. While conditions are such that this is an intentionally low probability Poisson occurrence ($\lambda < 0.01$), registry of the sample permits convenient return to and study of specific nanodimers identified by dark field microscopy or AFM. By way of example, an AFM image of such a nanohole dimer formed from two 60 nm nanoholes is shown in Figure 6A, along with the corresponding SPIM images of the same dimer under a variety of circular (B) and linear (C−F) polarization conditions. Due to the lower point group symmetry of the dimer, a strong polarization dependence is now observed, in which the photoemission signal peaks for laser polarization *perpendicular* to the dimer axis. This dependence is more quantitatively captured in the rightmost panel (Figure 6G), which reveals a sharply peaked angular distribution well described by $\cos^8(\theta)$. This is of course entirely consistent with (i) an $|E_0|\cdot\cos(\theta)$ projection of the incident field along the preferred photoemissivity direction, in conjunction with (ii) sensitivity in photoemission to the eighth power of the laser electric field enhancement factor $\eta_{ENH}(x,y)$. This angular behavior is also similar to the polarization dependence noted for gold nanorods, where the photoemission event is dominated by resonant plasmonic excitation along the rod long axis.[31]

Although the exact same plasmonic considerations are at play, the corresponding behavior for larger nanohole dimers (d = 500 nm) is fundamentally different, as summarized in Figure 7 for a near horizontal dimer alignment. Indeed, guided by the previous nanohole monomer studies, the reasonable expectation might be that, for circularly polarized excitation, the photoemission feature would cover the entire dimer structure and therefore be broadened *horizontally* by almost 2 × 500 nm =1000 nm. Instead, we experimentally see a *vertically* elongated feature, *perpendicular* to the dimer axis that is considerably smaller than the entire nanohole structure, with a horizontal fwhm closer to 450 nm (see Figure 7B). Second, similar to the behavior of large nanohole monomers, two peaks in the images are observed for linearly polarized excitation. Interestingly, however, these two peaks now maintain a *fixed* relative orientation *perpendicular* to the dimer axis, which *does not rotate* with the incident laser polarization, as illustrated in Figure 7C−F. However, the most dramatic change is in the integrated

dx.doi.org/10.1021/jp411943f | J. Phys. Chem. C 2014, 118, 6959−6971

Table 2. Peak COMSOL Field Enhancement Factors for Small ($d \approx 60$ nm $\ll \lambda$) and Large ($d \approx 500$ nm $\approx \lambda$) Nanohole Dimers and Laser Polarization Parallel/Perpendicular to the Dimer Axis[a]

Nanohole Dimer		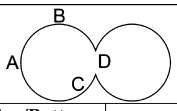			
Size	**Incident Polarization (Relative to Dimer Axis)**	**Left/Right Edge (A)**	**Top/Bottom Edge (B)**	**Wedge (C)**	**Cusp (D)**
Small	Parallel	**15**	4	4	<1
	Perpendicular	1.5	5	15	**180**
Large	Parallel	7	4	**12**	2
	Perpendicular	1	2	2	**9**

[a]A and B are regions of local curvature similar to the monomer in Table 1; C (wedge) and D (cusp) are unique to dimers, where largest enhancements are found. Note that the maximum value in *small* nanohole dimers is for *perpendicular* excitation at the *cusp*, while with *larger* dimers, the peak field enhancement is for *parallel* excitation in the vicinity of the *wedge*.

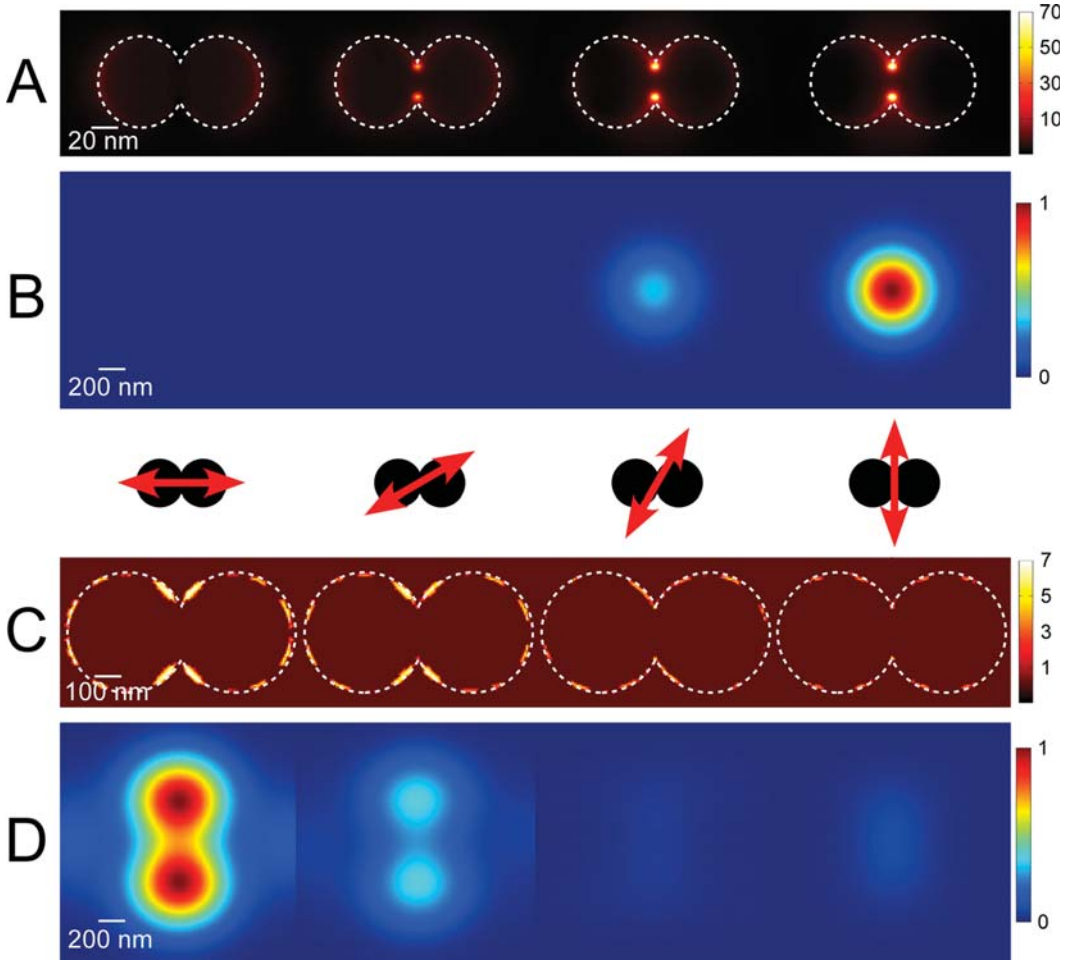

Figure 8. COMSOL simulations for a *small* ($d \approx 60$ nm $\ll \lambda$) nanohole dimer (upper panels) and a *large* ($d \approx 500$ nm $\approx \lambda$) nanohole dimer (lower panels) for selected polarizations shown schematically in the middle panel. (A) Field enhancement factor (η_{ENH}) for *small* nanohole dimers as a function of incident polarization (scale bar to right), with max $\eta_{ENH} \approx 180$ for *perpendicular* excitation in the cusp region. (B) SPIM predictions (η_{ENH}^{8} convoluted over the 2D incident electric field) normalized to max value over the full panel correctly reveal strong variation with polarization, but no anisotropy in the resulting image. (C) Spatial enhancement field images (η_{ENH}) for *large* nanohole dimers as a function of incident polarization (scale bar to right; peak $\eta_{ENH} \approx 12$ in wedge region for *parallel* excitation). (D) SPIM simulations predict polarization dependent intensity variations *opposite* to smaller nanohole dimers, as well as a spatial anisotropy *perpendicular* to the nanohole dimer axis. See Figure 5 and Tables 1 and 2 for further details and comparisons.

SPIM intensity as a function of incident laser polarization, as summarized in a polar plot in Figure 7G. Note that the AFM of this exact dimer is shown explicitly in Figure 7A, which is also in the same sample orientation as the subsequent SPIM images in Figure 7B–G. Remarkably, now the laser polarization alignment producing the highest photoelectron emission yield for the larger nanhole dimers is *parallel* to the dimer axis, i.e., exactly *opposite* to what is witnessed for the smaller nanohole dimers. Furthermore, the corresponding SPIM images reveal a clear propensity for spatial photoemission (i) from the *central*

dx.doi.org/10.1021/jp411943f | J. Phys. Chem. C 2014, 118, 6959–6971

region and (ii) along an axis *perpendicular* to the nanohole dimer. Such a major reversal in MPPE angular behavior for the larger (d = 500 nm) vs smaller (d = 60 nm) nanohole dimers suggests a qualitative difference in the physical site for electron photoemission, which we explore further below with COMSOL simulations.

B. Theory. Details of the dimer theoretical analysis are the same as previously discussed with respect to the nanohole monomers. Simulation of the local electric fields reveals the origin of the profound differences observed between the small and large dimers (Table 2). Figure 8A displays the calculated electric field enhancement for a small nanohole dimer upon excitation with various incident polarization directions relative to the dimer axis. Note that the color scales are all substantially expanded from those in Figure 5 (see caption). Enhancement factors for laser excitation parallel to the dimer axis (leftmost panel in Figure 8A) are ≈40, which are larger than, although still comparable to, the maximum values observed in the corresponding nanohole monomers.

However, what is even more remarkable is the dramatic increase in electric field enhancement as a function of laser polarization. For the case of perpendicular excitation, the COMSOL calculations predict an order of magnitude greater enhancement factor of $\eta_{ENH} \approx 400$. For a 4-photon photoemission process and a 10-fold difference in electric field enhancement factor, one therefore already predicts a 10^8-fold modulation in SPIM signals between horizontal and vertical polarization. This is nicely demonstrated in Figure 8B, which presents a spatial convolution of $(\eta_{ENH}(x,y))^8$ over the instrument response function, and thereby illustrates the enormous contrast in signal for excitation *perpendicular* vs *parallel* to the nanohole dimer axis. We note that this behavior is in excellent agreement with the polar SPIM data plot in Figure 6G, which is consistent with a perpendicular/parallel contrast in excess of 100:1.

The enhancement fields for the d = 500 nm nanohole dimers (Figure 8C) reveal many qualitative differences and similarities with respect to the d = 60 nm diffraction limited counterparts. Most importantly, the electric field enhancement factors are now maximized for excitation *parallel* to the dimer axis and in excellent agreement with what is observed experimentally. Indeed, although the hot spots are clearly predicted to be much more broadly distributed than in the case of the d = 60 nm nanodimer species, the region of greatest electric field enhancement still occurs predominantly near the dimer cusps. These regions along the sides of the cusp (i.e., wedges) become the source of strongest enhancement, with enhanced electric fields comparable to those observed at the cusps for the *orthogonal* laser polarization alignment. Additionally, the region over which the enhancement occurs is significantly larger in area, leading to greater integrated photoemission yield predicted for incident electric field *parallel* to the dimer axis, as shown in Figure 8D. The predicted images agree well with the experimental data presented in Figure 7, where the two peaks do not rotate with incident polarization. Furthermore, photoemission signals for excitation *perpendicular* to the dimer axis are predicted to be diminished with respect to *parallel* excitation, as indeed observed in the actual SPIM data images.

V. DISCUSSION

The multiphoton photoionization of isolated nanoholes provides many interesting results that reveal details on the local electric field enhancements of various structures. The easiest understood system is the nanohole monomer, as summarized in Figures 3 and 4. These simple structures reveal considerable differences in the MPPE spatial maps between small and large sizes. As expected, however, the total electron yield is experimentally found to be independent of incident polarization. Finite element electrodynamics simulations confirm this observation by revealing identical polarization dependence for the enhancement fields in the case of both small and large sizes. A clear spatial dependence upon changing polarization arises when the physical size of the nanohole monomer is included relative to the diffraction-limited resolution. The same spatial dependence has also been observed in related experiments using SHG in thick films (>100 nm Au) containing large (>500 nm diameter) holes.[37] Specifically, quite similar spatial maps were observed with peak SHG signal arising from nanohole edges perpendicular to the incident electric field vector. Note that the lower image resolution in earlier work arises due to the two-photon nature of the SHG technique, where signal is proportional to η_{ENH}^4 compared to η_{ENH}^8 in our case. As expected, the underlying spatial difference of the enhancement between small and large nanohole monomers is found to be quite minimal.

Nanohole dimers, on the other hand, provide a richer and more complex architecture with qualitative differences in the polarization dependent photoemission behavior observed both experimentally and theoretically. First of all, a strong dependence of total electron yield on laser polarization is experimentally observed for both small and large nanohole dimers, as identified in Figures 6 and 7. However, this dependence on laser polarization angle is clearly qualitatively different (specifically, shifted by 90°) for the small vs large nanohole dimer architecture, as also evident in Figures 6G and 7G. We can make a more quantitative comparison between our theoretical modeling and experimental results by closer inspection of the polarization dependence of the total photoelectron yield relative to the dimer axis. To be consistent with the experiment, the theoretical images are integrated at each angle to determine the total signal level from an individual nanohole dimer as a function of incident polarization, with the theoretical and experimental results summarized in Figure 9A,C

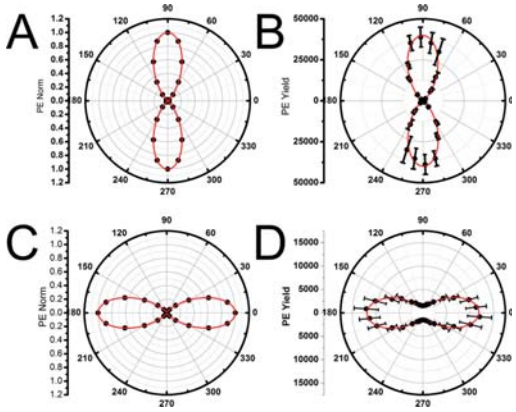

Figure 9. Theoretical (A, C) and experimental (B, D) polarization dependences for horizontally aligned nanohole dimers. Small nanohole dimers (60 nm, A) reveal a strongly *perpendicular* anisotropy, in excellent agreement with experiment (B). For the larger nanohole dimers (500 nm), theory (C) correctly predicts a predominantly *parallel* anisotropy in agreement with experiment (D), but underpredicts small nonzero contributions at *perpendicular* direction.

dx.doi.org/10.1021/jp411943f | J. Phys. Chem. C 2014, 118, 6959−6971

and Figure 9B,D for the small and large nanohole dimer, respectively. From a least-squares fit to $\cos^{2n}(\theta)$, theoretical results for the small nanohole dimers (Figure 9A) are found to be very closely proportional to $\cos^{8}(\theta)$, with a parallel/perpendicular contrast ratio in excess of $\sim 10^5$ for the two orthogonal directions. This is in excellent agreement with the experimental data (Figure 9B), which can also be nicely fit by a $\cos^{8}(\theta)$ distribution, as shown in the upper right panel. This can be most simply interpreted as arising from two facts: (i) that the photoionization process scales with the eighth power of the local electric field and (ii) that the plasmonic excitation for a small nanohole dimer below the diffraction limit arises from a single dipole-like excitation, similar to that previously observed in gold nanorods.[32]

The results for the large nanohole dimers are qualitatively similar but differ in two important ways. In the case of large nanohole dimers, the least-squares fits to the theoretical results predict a polarization dependence slightly better described by a $\cos^{7}(\theta)$ instead of $\cos^{8}(\theta)$ distribution. Simply stated, this is due to the longer range spatial extent of the predicted electric field enhancements, which brings the system further away from the strict dipole-like excitation limit and therefore slightly softens or blurs the angular dependence. This blurring is of course also true for excitation at the orthogonal polarization, which for any purely dipole-like dependence would be identically zero but in fact is now finite. Indeed, as shown in Figure 8C, this is due to the presence of nonzero electric field enhancement factors for both polarizations. We can take this into account by summing a constant isotropic term into our $\cos^{7}(\theta)$ model, which yields theoretical contrast between the two orthogonal directions only on the order of ~50:1. Though small, the presence of such an isotropic term is clearly real, as can be seen in the experimental data for the large nanohole dimer in Figure 9D. Consistent with our treatment of the theoretical predictions, the red line represents a similar fit to a $\cos^{7}(\theta)$ distribution superposed with an additional angle independent term. Note that the magnitude of the isotropic offset observed experimentally is considerably larger (approximately a factor of 10) than that predicted by the theory, but the $\cos^{7}(\theta)$ angular dependence is described relatively well.

In contrast with monomer-based architectures, the corresponding nanoparticle dimers are often found to behave rather uniquely in many experimental venues, such as luminescence,[54] fluorescence enhancement of molecules,[55] or surface enhanced Raman scattering.[9,14,56,57] One often quoted reason for the unusually high photophysical activity of dimers is that the physical gap between dimers is where the largest enhancement fields are predicted to be observed.[58−60] Moerner and co-workers exploited this local electric field enhancement in bowtie nanoantennas to detect single molecule fluorescence, implying enhancement factors as large as 1340.[55] High local electric fields have also been suggested to generate ion fluorescence in the extreme-ultraviolet (λ = 47 nm) from a bowtie nanoantenna array with an enhancement factor of near 380,[61−64] with initial claims of the EUV arising from high harmonic generation not fully resolved.[65] Other closely related systems are the triangular "bowtie apertures", which have been studied thoroughly by Xu and co-workers with near-field methods and which reveal maximal electric field for laser polarization aligned across the gap.[66−69] One common feature in all these previous studies is the nanoparticle size; these bowtie structures, typically with less than 100 nm edge lengths, are most comparable to our 60 nm nanohole dimers. One might therefore expect a similar electric field enhancement behavior in the 60 nm nanohole dimers to that seen in bowtie systems, since an effective bowtie is formed in our architectures by the gap structure located at the cusps. From such a picture, the most intense local electric field enhancement factors would be achieved when the incident polarization is *perpendicular* to the dimer axis, and therefore aligned with the gap, which is in excellent agreement with both experimental photoemission yields and theoretical predictions.

Though clearly governed by the same plasmonic physics, the larger nanohole dimers behave quite differently, where now the strongest total electron yield occurs for incident electric field *parallel* rather than perpendicular to the dimer axis. It is still the case that the bowtie type excitation of the cusp regions is present for excitation perpendicular to the dimer axis; however, excitation *parallel* to the large nanohole dimer axis results in enhancement factors of at least comparable magnitude. Furthermore, as discussed previously, the total electron yield is determined not merely by the absolute magnitude of these enhancement factors but also by the effective photoemission area over which this occurs. Indeed, this latter contribution proves to be the dominant reason for the different polarization dependent photoemission behavior between the large and small nanohole dimers. This is beautifully confirmed by the COMSOL calculations shown in Figure 8C, which reveal a very strong and highly localized hot spot in electric field enhancement precisely at the bowtie-like cusps for perpendicular excitation (right side panel), but which is simply overwhelmed by the much larger areas of comparable electric field enhancement at the wedges obtained for parallel excitation (left side panel). This is in good agreement with the effect observed in SHG studies from large (>500 nm diameter) dimers in thick films by Onuta et al.[37] In these studies, nearly equal SHG signal intensities were noted for this two-photon process upon both parallel and perpendicular excitation directions, with spatial maps resembling those in Figure 8C. This further supports that nanohole dimer structures with dimensions near or above the diffraction limit can lead to local field enhancement patterns fundamentally quite different from those of smaller nanohole dimers, where more purely dipole-like excitation patterns prevail.

As a final comment, it is also worth noting that neither small nor large nanohole dimers behave as a simple linear combination of two nanohole monomers. By way of example, consider two touching nanoholes aligned horizontally, as shown in Table 2. For vertically polarized excitation, i.e., perpendicular to the dimer axis, the simple superposition of two monomers would lead to a pair of enhancement fields located at the upper and lower curved regions and displaced by the nanohole diameter (i.e., region B with corresponding symmetry reflections). By way of contrast, the COMSOL simulations predict the region of maximum electric field enhancements to be at the cusps (region D) for small dimers or an expanded area surrounding the cusps (regions D and C) for the larger dimers. In neither size limit is the maximum enhancement localized around region B. Alternatively, if we consider excitation *parallel* to the dimer axis, a simple superposition expectation would be for the left/right edges (region A and its mirror image) to be most intense. For the small nanohole dimer, this is indeed where the local electric fields are maximal: albeit at approximately half of the isolated nanohole value. On the other hand, the left/right electric field enhancement regions for the large nanohole dimers are now considerably weaker than

the cusp regions and thus do not contribute significantly to the spatial photoemission images observed. Of course, this is not any violation of the superposition principle, which is exact for static fields, but simply a matter of retardation effects for optical fields with nanoarchitectures near or above the diffraction limit. Nevertheless, this clearly supports that overlapping and nonoverlapping dimer structures can be quite different. In fact, studies have confirmed that the transition in electric field behavior from nearly touching to electrically contacted nanoobjects can even be discontinuous and therefore lead to unusual plasmonic behavior.[70,71] In any event, the present comparison between scanning photoelectron emission microscopy and COMSOL calculations for nanohole monomers and dimers provides benchmark examples of the underlying electric field enhancement dynamics of such simple yet novel plasmonic architectures.

VI. SUMMARY

Metal nanoholes and nanohole dimers formed by shadow mask lithography on Au films have been exploited as unique nanoobjects for investigating multiphoton photoemission (MPPE) from plasmonic materials, as well as simple yet tractable test systems for direct calculation of plasmonic near-field enhancements. Small nanoholes substantially below the diffraction limit ($d \ll \lambda$) are found to yield significant electric field enhancements both parallel ($\eta_{ENH} \approx 20$) and perpendicular ($\eta_{ENH} \approx 5$) to the laser polarization axis. These enhancements are responsible for producing strong scanning photoionization microscopy (SPIM) signals under conditions of ultrafast laser excitation, with overall photoemission yield exhibiting isotropic dependence on laser polarization due to a combination of (i) sub-diffraction limited size and (ii) near perfect azimuthal symmetry. Corresponding studies of nanoholes with sizes near the diffraction limit ($d \approx \lambda$) also reveal large electric field enhancements near tangent edges of the cylindrical hole aligned *perpendicular to* the laser polarization. Since the larger nanohole diameters are now comparable to the excitation wavelength, the photoelectron source regions can be clearly resolved in SPIM image maps as two lobes that (i) are parallel to and (ii) rotate with the incident electric field polarization. However, the *integrated* SPIM photoemission signal magnitudes for both small and large nanohole monomers remain completely isotropic with respect to polarization angle by virtue of azimuthal symmetry. Predictions of a simple model based on (i) detailed COMSOL simulations of the electric near field η_{ENH}, (ii) sensitivity of a 4-photon photoemission process ($n = 4$) on η_{ENH} raised to the $(2n)$th power, and (iii) properly accounted for instrument response function prove to be in outstanding agreement with the experimental data.

Subsequent reduction of the azimuthal symmetry for nanohole dimers reveals a significantly richer spectrum of plasmonic and photoemission behavior, which we have explored for the two limiting cases of small ($d \ll \lambda$) and large ($d \approx \lambda$) holes. COMSOL simulations of the electric fields around these dimer nanostructures reveal strongly spatially dependent enhancement fields that vary sensitively with incident polarization. Small nanohole dimers are found to behave qualitatively like "bowtie" nanoantennas of Moerner and co-workers, whereby the enhancement field is largest at the central cusps for laser polarization *perpendicular* to the dimer axis.[55] This is in clear contrast to the larger nanohole dimers, which exhibit pronounced photoemission signals from regions around the cusp edges, but which are primarily excited for polarization vectors *parallel* to the dimer axis. In all cases, the same model of field enhancement raised to the eighth power (η_{ENH}^8) convolved over the instrument response function yields excellent agreement with all experimental data. As one critical factor in the SPIM image predictions, maximum photoemission yield is found to depend not only on the *magnitude* of the local field enhancement to the eighth power but also on the relative areas for potential photoelectron emission over which this enhancement occurs.

Directions for future studies include experimental and theoretical studies into the size regime between small (60 nm) and large (500 nm) dimers, where the polarization dependence of the maximum photoemission signals is found to transition from *perpendicular* to *parallel* with respect to the dimer axis. Additionally, it would be quite interesting to further study the wavelength dependence of the SPIM signals, in order to correlate (i) near field MPPE wavelength dependence with (ii) the far field scattering spectra and thereby further investigate the synergism between near field enhancement, photoemissivity, and far field optical properties. Lastly, these nanohole lithography methods can be simply extended with off-axis metallic film deposition to formation of nearly perfect elliptical holes, which should of course exhibit additional sensitivity to wavelength and polarization of the photoemission laser light. In summary, the ability to both (i) measure photoemission from nanoobjects with SPIM and (ii) model the detailed plasmonic response of these species from first principles electrodynamics calculations opens a wealth of new opportunities for exploring near-field characteristics of nanosystems with spatial resolution that extends far below the conventional diffraction limit.

AUTHOR INFORMATION

Notes

The authors declare no competing financial interest.

ACKNOWLEDGMENTS

This work has been supported by the Air Force Office of Scientific Research (FA9550-12-1-0139), with additional funds for optics, microscopy, and computer resources provided by the National Science Foundation (CHE1012685, PHYS1125844) and the National Institute for Standards and Technology. We also gratefully acknowledge D. Alchenberger for help with the metal deposition.

REFERENCES

(1) Mock, J. J.; Barbic, M.; Smith, D. R.; Schultz, D. A.; Schultz, S. Shape Effects in Plasmon Resonance of Individual Colloidal Silver Nanoparticles. *J. Chem. Phys.* **2002**, *116*, 6755−6759.

(2) Emory, S. R.; Nie, S. Screening and Enrichment of Metal Nanoparticles with Novel Optical Properties. *J. Phys. Chem. B* **1998**, *102*, 493−497.

(3) Kelly, K. L.; Coronado, E.; Zhao, L. L.; Schatz, G. C. The Optical Properties of Metal Nanoparticles: The Influence of Size, Shape, and Dielectric Environment. *J. Phys. Chem. B* **2003**, *107*, 668−677.

(4) Wiley, B. J.; Im, S. H.; Li, Z. Y.; McLellan, J.; Siekkinen, A.; Xia, Y. A. Maneuvering the Surface Plasmon Resonance of Silver Nanostructures Through Shape-Controlled Synthesis. *J. Phys. Chem. B* **2006**, *110*, 15666−15675.

(5) Brolo, A. G.; Gordon, R.; Leathem, B.; Kavanagh, K. L. Surface Plasmon Sensor Based on the Enhanced Light Transmission Through Arrays of Nanoholes in Gold Films. *Langmuir* **2004**, *20*, 4813−4815.

(6) Charbonneau, R.; Lahoud, N. Demonstration of Integrated Optics Elements Based on Long-Ranging Surface Plasmon Polaritons. *Opt. Express* **2005**, *13*, 977−984.
(7) Haes, A. J.; Zou, S. L.; Schatz, G. C.; Van Duyne, R. P. Nanoscale Optical Biosensor: Short Range Distance Dependence of the Localized Surface Plasmon Resonance of Noble Metal Nanoparticles. *J. Phys. Chem. B* **2004**, *108*, 6961−6968.
(8) Lee, K. S.; El-Sayed, M. A. Gold and Silver Nanoparticles in Sensing and Imaging: Sensitivity of Plasmon Response to Size, Shape, and Metal Composition. *J. Phys. Chem. B* **2006**, *110*, 19220−19225.
(9) Michaels, A. M.; Nirmal, M.; Brus, L. E. Surface Enhanced Raman Spectroscopy of Individual Rhodamine 6G Molecules on Large Ag Nanocrystals. *J. Am. Chem. Soc.* **1999**, *121*, 9932−9939.
(10) Srituravanich, W.; Fang, N.; Sun, C.; Luo, Q.; Zhang, X. Plasmonic Nanolithography. *Nano Lett.* **2004**, *4*, 1085−1088.
(11) Camden, J. P.; Dieringer, J. A.; Wang, Y. M.; Masiello, D. J.; Marks, L. D.; Schatz, G. C.; Van Duyne, R. P. Probing the Structure of Single-Molecule Surface-Enhanced Raman Scattering Hot Spots. *J. Am. Chem. Soc.* **2008**, *130*, 12616−12617.
(12) Ciou, S. H.; Cao, Y. W.; Huang, H. C.; Su, D. Y.; Huang, C. L. Sers Enhancement Factors Studies of Silver Nanoprism and Spherical Nanoparticle Colloids in the Presence of Bromide Ions. *J. Phys. Chem. C* **2009**, *113*, 9520−9525.
(13) Dieringer, J. A.; Wustholz, K. L.; Masiello, D. J.; Camden, J. P.; Kleinman, S. L.; Schatz, G. C.; Van Duyne, R. P. Surface-Enhanced Raman Excitation Spectroscopy of a Single Rhodamine 6G Molecule. *J. Am. Chem. Soc.* **2009**, *131*, 849−854.
(14) Jiang, J.; Bosnick, K.; Maillard, M.; Brus, L. Single Molecule Raman Spectroscopy at the Junctions of Large Ag Nanocrystals. *J. Phys. Chem. B* **2003**, *107*, 9964−9972.
(15) Moskovits, M. Surface-Enhanced Raman Spectroscopy: A Brief Perspective. In *Surface-Enhanced Raman Scattering: Physics and Applications*; Kneipp, K., Moskovits, M., Kneipp, H., Eds.; Springer: Berlin, 2006; Vol. *103*, 1−17
(16) Berthelot, J.; Bachelier, G.; Song, M. X.; Rai, P.; des Francs, G. C.; Dereux, A.; Bouhelier, A. Silencing and Enhancement of Second-Harmonic Generation in Optical Gap Antennas. *Opt. Express* **2012**, *20*, 10498−10508.
(17) Kroo, N.; Farkas, G.; Dombi, P.; Varro, S. Nonlinear Processes Induced by the Enhanced, Evanescent Field of Surface Plasmons Excited by Femtosecond Laser Pulses. *Opt. Express* **2008**, *16*, 21656−21661.
(18) Park, S.; Hahn, J. W.; Lee, J. Y. Doubly Resonant Metallic Nanostructure for High Conversion Efficiency of Second Harmonic Generation. *Opt. Express* **2012**, *20*, 4856−4870.
(19) Slablab, A.; Le Xuan, L.; Zielinski, M.; de Wilde, Y.; Jacques, V.; Chauvat, D.; Roch, J. F. Second-Harmonic Generation from Coupled Plasmon Modes in a Single Dimer of Gold Nanospheres. *Opt. Express* **2012**, *20*, 220−227.
(20) Aers, G. C.; Inglesfield, J. E. Photoyield Enhancement from Small Metal Particles. *J. Phys. F: Met. Phys.* **1983**, *13*, 1743.
(21) Endriz, J. G. Calculation of the Surface Photoelectric Effect. *Phys. Rev. B* **1973**, *7*, 3464−3481.
(22) Endriz, J. G.; Spicer, W. E. Study of Aluminum Films. II. Photoemission Studies of Surface-Plasmon Oscillations on Controlled-Roughness Films. *Phys. Rev. B* **1971**, *4*, 4159−4184.
(23) Kubo, A.; Onda, K.; Petek, H.; Sun, Z. J.; Jung, Y. S.; Kim, H. K. Femtosecond Imaging of Surface Plasmon Dynamics in a Nanostructured Silver Film. *Nano Lett.* **2005**, *5*, 1123−1127.
(24) Petek, H.; Ogawa, S. Femtosecond Time-Resolved Two-Photon Photoemission Studies of Electron Dynamics in Metals. *Prog. Surf. Sci.* **1997**, *56*, 239−310.
(25) Douillard, L.; Charra, F. High-Resolution Mapping of Plasmonic Modes: Photoemission and Scanning Tunnelling Luminescence Microscopies. *J. Phys. D: Appl. Phys.* **2011**, *44*, 464002.
(26) Gloskovskii, A.; Valdaitsev, D. A.; Cinchetti, M.; Nepijko, S. A.; Lange, J.; Aeschlimann, M.; Bauer, M.; Klimenkov, M.; Viduta, L. V.; Tomchuk, P. M.; Schonhense, G. Electron Emission from Films of Ag and Au Nanoparticles Excited by a Femtosecond Pump-Probe Laser. *Phys. Rev. B* **2008**, *77*, 195427.
(27) Hrelescu, C.; Sau, T. K.; Rogach, A. L.; Jaeckel, F.; Laurent, G.; Douillard, L.; Charra, F. Selective Excitation of Individual Plasmonic Hotspots at the Tips of Single Gold Nanostars. *Nano Lett.* **2011**, *11*, 402−407.
(28) Cinchetti, M.; Gloskovskii, A.; Nepjiko, S. A.; Schonhense, G.; Rochholz, H.; Kreiter, M. Photoemission Electron Microscopy as a Tool for the Investigation of Optical Near Fields. *Phys. Rev. Lett.* **2005**, *95*, 047601.
(29) Schertz, F.; Schmelzeisen, M.; Mohammadi, R.; Kreiter, M.; Elmers, H.-J.; Schoenhense, G. Near Field of Strongly Coupled Plasmons: Uncovering Dark Modes. *Nano Lett.* **2012**, *12*, 1885−1890.
(30) Grubisic, A.; Mukherjee, S.; Halas, N.; Nesbitt, D. J. Anomalously Strong Electric Near-Field Enhancements at Defect Sites on AuNanoshells Observed by Ultrafast Scanning Photoemission Imaging Microscopy. *J. Phys. Chem. C* **2013**, *117*, 22545−22559.
(31) Schweikhard, V.; Grubisic, A.; Baker, T. A.; Thomann, I.; Nesbitt, D. J. Polarization-Dependent Scanning Photoionization Microscopy: Ultrafast Plasmon-Mediated Electron Ejection Dynamics in Single Au Nanorods. *ACS Nano* **2011**, *5*, 3724−3735.
(32) Grubisic, A.; Schweikhard, V.; Baker, T. A.; Nesbitt, D. J. Coherent Multiphoton Photoelectron Emission from Single Au Nanorods: The Critical Role of Plasmonic Electric Near-Field Enhancement. *ACS Nano* **2013**, *7*, 87−99.
(33) Grubisic, A.; Ringe, E.; Cobley, C. M.; Xia, Y.; Marks, L. D.; Van Duyne, R. P.; Nesbitt, D. J. Plasmonic near-Electric Field Enhancement Effects in Ultrafast Photoelectron Emission: Correlated Spatial and Laser Polarization Microscopy Studies of Individual Ag Nanocubes. *Nano Lett.* **2012**, *12*, 4823−4829.
(34) Prikulis, J.; Hanarp, P.; Olofsson, L.; Sutherland, D.; Käll, M. Optical Spectroscopy of Nanometric Holes in Thin Gold Films. *Nano Lett.* **2004**, *4*, 1003−1007.
(35) Sepulveda, B.; Alaverdyan, Y.; Alegret, J.; Käll, M.; Johansson, P. Shape Effects in the Localized Surface Plasmon Resonance of Single Nanoholes in Thin Metal Films. *Opt. Express* **2008**, *16*, 5609−5616.
(36) Apell, S. P.; Echenique, P. M.; Ritchie, R. H. Sum Rules for Surface Plasmon Frequencies. *Ultramicroscopy* **1996**, *65*, 53−60.
(37) Onuta, T.-D.; Waegele, M.; DuFort, C. C.; Schaich, W. L.; Dragnea, B. Optical Field Enhancement at Cusps Between Adjacent Nanoapertures. *Nano Lett.* **2007**, *7*, 557−564.
(38) Jones, M. R.; Osberg, K. D.; Macfarlane, R. J.; Langille, M. R.; Mirkin, C. A. Templated Techniques for the Synthesis and Assembly of Plasmonic Nanostructures. *Chem. Rev.* **2011**, *111*, 3736−3827.
(39) Sannomiya, T.; Scholder, O.; Jefimovs, K.; Hafner, C.; Dahlin, A. B. Investigation of Plasmon Resonances in Metal Films with Nanohole Arrays for Biosensing Applications. *Small* **2011**, *7*, 1653−1663.
(40) Zhang, X. Y.; Whitney, A. V.; Zhao, J.; Hicks, E. M.; Van Duyne, R. P. Advances in Contemporary Nanosphere Lithographic Techniques. *J. Nanosci. Nanotechnol.* **2006**, *6*, 1920−1934.
(41) Haynes, C. L.; McFarland, A. D.; Smith, M. T.; Hulteen, J. C.; Van Duyne, R. P. Angle-Resolved Nanosphere Lithography: Manipulation of Nanoparticle Size, Shape, and Interparticle Spacing. *J. Phys. Chem. B* **2002**, *106*, 1898−1902.
(42) Fredriksson, H.; Alaverdyan, Y.; Dmitriev, A.; Langhammer, C.; Sutherland, D. S.; Zäch, M.; Kasemo, B. Hole−Mask Colloidal Lithography. *Adv. Mater.* **2007**, *19*, 4297−4302.
(43) Haynes, C. L.; Van Duyne, R. P. Nanosphere Lithography: A Versatile Nanofabrication Tool for Studies of Size-Dependent Nanoparticle Optics. *J. Phys. Chem. B* **2001**, *105*, 5599−5611.
(44) Monti, O. L. A.; Baker, T. A.; Nesbitt, D. J. Imaging Nanostructures with Scanning Photoionization Microscopy. *J. Chem. Phys.* **2006**, *125*, 154709.
(45) Schweikhard, V.; Grubisic, A.; Baker, T. A.; Nesbitt, D. J. Multiphoton Scanning Photoionization Imaging Microscopy for Single-Particle Studies of Plasmonic Metal Nanostructures. *J. Phys. Chem. C* **2011**, *115*, 83−91.

(46) Michaelson, H. B. The Work Function of the Elements and Its Periodicity. *J. Appl. Phys.* **1977**, *48*, 4729−4733.
(47) Johnson, P. B.; Christy, R. W. Optical Constants of the Noble Metals. *Phys. Rev. B* **1972**, *6*, 4370−4379.
(48) Pors, A.; Albrektsen, O.; Bozhevolnyi, S. I.; Willatzen, M. The Optical Properties of a Truncated Spherical Cavity Embedded in Gold. In *Proceedings of the COMSOL Conference 2009 Milan*; 2009.
(49) Rindzevicius, T.; Alaverdyan, Y.; Sepulveda, B.; Pakizeh, T.; Käll, M.; Hillenbrand, R.; Aizpurua, J.; Garcia de Abajo, F. J. Nanohole Plasmons in Optically Thin Gold Films. *J. Phys. Chem. C* **2007**, *111*, 1207−1212.
(50) Schwind, M.; Kasemo, B.; Zoric, I. Localized and Propagating Plasmons in Metal Films with Nanoholes. *Nano Lett.* **2013**, *13*, 1743−1750.
(51) Dreier, J.; Eriksen, R. L.; Albrektsen, O.; Pors, A.; Simonsen, A. C. Gold Films with Imprinted Cavities. *J. Phys. Chem. Lett.* **2009**, *1*, 260−264.
(52) Knight, M. W.; Halas, N. J. Nanoshells to Nanoeggs to Nanocups: Optical Properties of Reduced Symmetry Core−Shell Nanoparticles Beyond the Quasistatic Limit. *New J. Phys.* **2008**, *10*, 105006.
(53) Wu, L. Y.; Ross, B. M.; Lee, L. P. Optical Properties of the Crescent-Shaped Nanohole Antenna. *Nano Lett.* **2009**, *9*, 1956−1961.
(54) Wu, E.; Chi, Y.; Wu, B.; Xia, K.; Yokota, Y.; Ueno, K.; Misawa, H.; Zeng, H. Spatial Polarization Sensitivity of Single Au Bowtie Nanostructures. *J. Lumin.* **2011**, *131*, 1971−1974.
(55) Kinkhabwala, A.; Yu, Z.; Fan, S.; Avlasevich, Y.; Muellen, K.; Moerner, W. E. Large Single-Molecule Fluorescence Enhancements Produced by a Bowtie Nanoantenna. *Nat. Photonics* **2009**, *3*, 654−657.
(56) Michaels, A. M.; Jiang, J.; Brus, L. Ag Nanocrystal Junctions as the Site for Surface-Enhanced Raman Scattering of Single Rhodamine 6G Molecules. *J. Phys. Chem. B* **2000**, *104*, 11965−11971.
(57) Xu, H.; Käll, M. Polarization-Dependent Surface-Enhanced Raman Spectroscopy of Isolated Silver Nanoaggregates. *ChemPhysChem* **2003**, *4*, 1001−1005.
(58) Zhang, X. Y.; Hicks, E. M.; Zhao, J.; Schatz, G. C.; Van Duyne, R. P. Electrochemical Tuning of Silver Nanoparticles Fabricated by Nanosphere Lithography. *Nano Lett.* **2005**, *5*, 1503−1507.
(59) Hao, E.; Schatz, G. C. Electromagnetic Fields around Silver Nanoparticles and Dimers. *J. Chem. Phys.* **2004**, *120*, 357−366.
(60) McMahon, J. M.; Henry, A. I.; Wustholz, K. L.; Natan, M. J.; Freeman, R. G.; Van Duyne, R. P.; Schatz, G. C. Gold Nanoparticle Dimer Plasmonics: Finite Element Method Calculations of the Electromagnetic Enhancement to Surface-Enhanced Raman Spectroscopy. *Anal. Bioanal. Chem.* **2009**, *394*, 1819−1825.
(61) Kim, S.; Jin, J.; Kim, Y.-J.; Park, I.-Y.; Kim, Y.; Kim, S.-W. High-Harmonic Generation by Resonant Plasmon Field Enhancement. *Nature* **2008**, *453*, 757−760.
(62) Sivis, M.; Duwe, M.; Abel, B.; Ropers, C. Extreme-Ultraviolet Light Generation in Plasmonic Nanostructures. *Nat. Phys.* **2013**, *9*, 304−309.
(63) Sivis, M.; Duwe, M.; Abel, B.; Ropers, C. Nanostructure-Enhanced Atomic Line Emission. *Nature* **2012**, *485*, E1−E3.
(64) Kim, S.; Jin, J.; Kim, Y.-J.; Park, I.-Y.; Kim, Y.; Kim, S.-W.; et al. Reply. *Nature* **2012**, *485*, E1−E3.
(65) Raschke, M. B. High-Harmonic Generation with Plasmonics: Feasible or Unphysical? *Ann. Phys. (Berlin)* **2013**, *525*, A40−A42.
(66) Jin, E. X.; Xu, X. F. Enhanced Optical Near Field from a Bowtie Aperture. *Appl. Phys. Lett.* **2006**, *88*, 153110.
(67) Jin, E. X.; Xu, X. Optical Resonance in Bowtie-Shaped Nanoapertures. *J. Comput. Theor. Nanosci.* **2008**, *5*, 214−220.
(68) Jin, E. X.; Xu, X. Plasmonic Effects in Near-Field Optical Transmission Enhancement Through a Single Bowtie-Shaped Aperture. *Appl. Phys. B* **2006**, *84*, 3−9.
(69) Sendur, K.; Challener, W. Near-Field Radiation of Bow-Tie Antennas and Apertures at Optical Frequencies. *J. Microscopy* **2003**, *210*, 279−283.
(70) Atay, T.; Song, J. H.; Nurmikko, A. V. Strongly Interacting Plasmon Nanoparticle Pairs: From Dipole-Dipole Interaction to Conductively Coupled Regime. *Nano Lett.* **2004**, *4*, 1627−1631.
(71) Romero, I.; Aizpurua, J.; Bryant, G. W.; Garcia de Abajo, F. J. Plasmons in Nearly Touching Metallic Nanoparticles: Singular Response in the Limit of Touching Dimers. *Opt. Express* **2006**, *14*, 9988−9999.